Chapter 13

Laser Ablation of Energetic Materials

Ruiqi Shen, Lizhi Wu, Wei Zhang and Haonan Zhang

Additional information is available at the end of the chapter

http://dx.doi.org/10.5772/intechopen.71892

Abstract

The initiation of explosives by laser is a new initiation method. Compared with traditional initiation methods, laser initiation has the characteristics of high reliability and high safety. It can be used as one of the alternative technologies for future initiation device. A microscopic understanding of the complex physical and chemical processes involved in the reaction process is essential for laser initiation. Shock initiation technology of laser-driven flyer was studied. Several typical laser-driven flyer targets researches were introduced. Some significant characteristics including velocity and impact stress of flyers were tested via photonic Doppler velocimetry and polyvinylidene fluoride pressure sensor, respectively. Some types of flyers including Al and Cu single-layer flyers and CuO/Cu, CuO/Al, and CuO/Al/Cu multilayer flyers with relatively high velocities were used to initiate PETN explosive. In order to give a better understanding of the mechanism of laser interaction with typical energetic materials (RDX, HMX, TNT, and HNS), a time of flight mass spectrometer (TOFMS) was used to detect the positive ions and the negative ions were produced in the laser-induced dissociation processes. The influences of laser wavelength, the laser fluence, and the delay time of the decomposition process have been studied as well. The results may throw some light on the laser interaction mechanism of energetic materials.

Keywords: laser ablation, PDV, laser-driven flyer, TOFMS, nitramines, aromatic nitro compounds

1. Introduction

Laser ablation of energetic materials, such as pyrotechnics, explosives, and propellants, is different from other materials because of the interaction with chemical reaction and laser beam. The interaction processes between energetic material and laser beam are accompanied with thermal physics process irradiated by laser (photo-thermal, melting, and gasification),

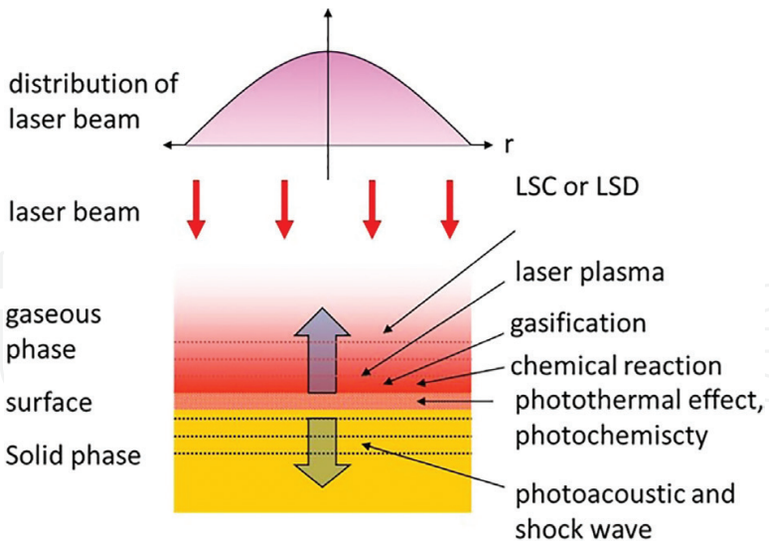

Figure 1. Interaction mechanism between laser beam and energetic materials.

chemical reaction in condensed phase and gaseous phase, generation of plasma, and laser-supported combustion (LSC) and laser-supported detonation (LSD) depending on laser power and material characteristics, seen in **Figure 1**.

Laser ablation of energetic materials is different from other materials' in chemical reaction, in which the chemical reactions in condensed and gaseous phase can induce ignition, combustion, and/or detonation. The research results show the reaction irradiated by laser is attributed to the category of thermochemistry at low power ($<10^3 W/mm^2$), but it is a complex reaction including laser ablation and laser plasma at high power ($>10^3 W/mm^2$).

2. Shock initiation technology of laser-driven flyer

As a type of driving energy, laser is able to ablate the target to generate substances with high temperature and pressure to propel objects up to high velocity. There exist mainly two modes of laser-driven flyers including inward driving and linear driving as shown in **Figure 2**.

Figure 2(a) shows an inward driving structure with free outward spherical surface as target. After being ablated by intense laser (with intensity of light over 10^{12} $W \cdot cm^{-2}$), the target will be disaggregated as plasmas with high temperature, high pressure, and high density to promote the rest part of target shell to be a flyer with high velocity. Immediately, the high-velocity flyer will cause implosion of deuterium and tritium medium inside the shell to achieve compressed fusion ignition (CFI). In linear driving structure shown in **Figure 2(b)**, the incident surface is covered by the transparent substrate or the optical fiber. If the intensity of incident laser is not that high (10^9–10^{11} $W \cdot cm^{-2}$), the transparent substrate can block the expansion of plasmas temporarily to enhance the impact stress and velocity of flyer (the remainder of target plate after ablation). This chapter mainly focuses on laser-driven flyer technology based on transparent substrate, which is gradually becoming a significant dynamic high pressure loading technology.

The process of laser-driven flyer is very complex and can be roughly divided into several steps as follows. First, the laser beam penetrates into the transparent substrate and irradiates on the

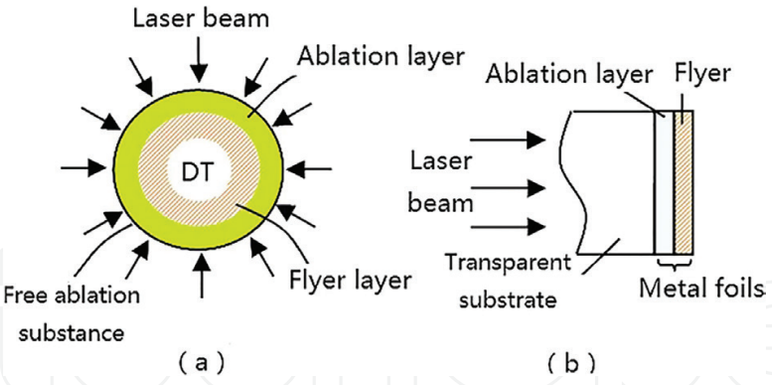

Figure 2. Two modes of laser-driven flyers: (a) inward driving (b) linear driving.

surface of the metal film, so that the film substance is heated and evaporated. Then, the plasmas formed at the interface between substrate and metal absorb the laser energy continuously to heat up and expand. Next, the rest part of metal film is released out to form high-velocity flyer.

Compared with conventional high-velocity driving methods including gas cannon, detonation, and electromagnetic driving, laser-driven flyer shows advantages of greatly enhancing the velocity of flyer (up to tens of km/s) and impact stress (up to TPa order), owning simple structure and low cost. Therefore, laser-driven technology is widely used in high-pressure physics, space science, material science, and research of rapid detonation for explosives [1].

Laser-driven flyer impact initiation technology is an application of laser-driven flyer, which is the process of initiating high energy explosives with high-velocity flyer driven by laser. As shown in **Figure 3**, the process of laser-driven flyer initiating explosive can be divided into three main steps:

a. The laser beam penetrates into the transparent substrate and interacts with the film on the back of substrate so that a part of film material is ablated instantaneously to form plasmas, which can absorb the laser energy unceasingly,

b. The plasmas with high temperature and high pressure can only expand in the direction of the film material due to the confinement of substrate so that the remaining nonablated films are sheared down to form high-velocity flyer, which is accelerated in accelerating chamber immediately,

c. The flying flyer at high velocity impacts on explosive surface and causes detonation to initiate explosive (e.g. HNS and PETN).

It is the precise time control, rapid response, strong electromagnetic interference resistance, and low sensitivity that makes laser-driven flyer impact initiation technology as a good potential for the application to modern fuze system.

2.1. Laser-driven flyer target

At present, the flying target with transparent substrate is mainly used in laser-driven flyer impact initiation technology due to its great performance of enhancing the absorption of laser energy by plasma and increasing the impact momentum of flyer. Usually, BK7, K9, or

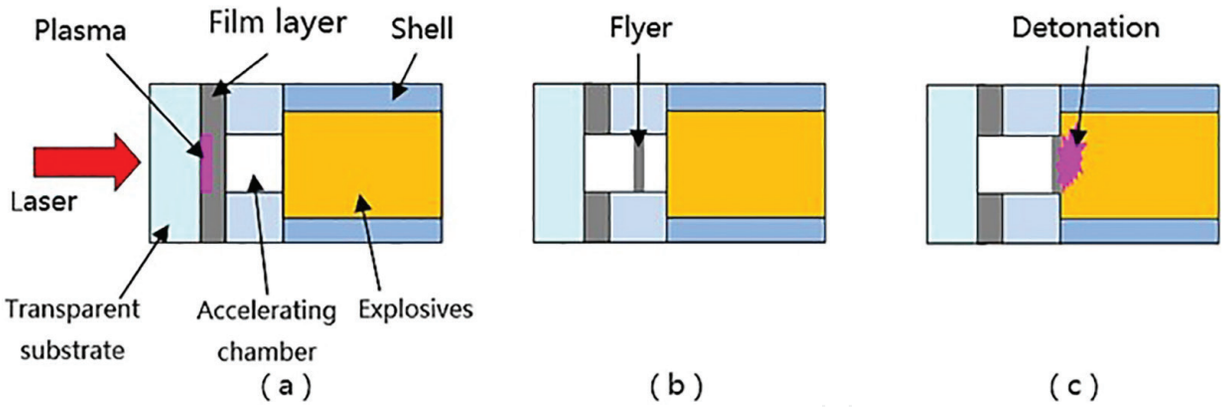

Figure 3. Process of laser-driven flyer impact initiation.

sapphire glass with high transmittance of the corresponding wavelength are adopted as the transparent substrate.

In general, thickness of the film deposited on the transparent substrate is typically a few microns to tens of microns and the diameter is about 1 mm. Paisley et al. [2] found that the impact stress of flyer must be higher than the rarefaction wave's reflected from the free surface of flyer during plasma-driving laser ablation. Only under this condition the flyer continue to be accelerated to reach the final velocity. In addition, the laser pulse width must be 2.5 times larger than round-trip time of sound in the flyer in order to ensure that the flyer will not be fully impacted, ablated, and chipped during the acceleration.

$$R = T/\left[\sim 2.5\left(2t/C_1\right)\right], \text{ that is } R = \frac{0.2\left(TC_1\right)}{t} \tag{1}$$

In Eq. (1), the dimensionless quantity R must be greater than 1, T (s) is the laser pulse width, t (mm) is the thickness of flyer, C_1 (mm/s) is the radial sound velocity of flyer.

2.1.1. Structure of flyer target

The structure of flyer target can be divided into two types: single-layer flyer and multilayer flyer. **Figure 4(a)** shows the structure of single-layer flyer. As we can see, single-layer flyer is prepared by depositing metal film on the transparent substrate. After the interaction between laser and metal film, the plasma with high temperature and high pressure produced through ablation will drive the nonablated film and shear it out to form a flyer.

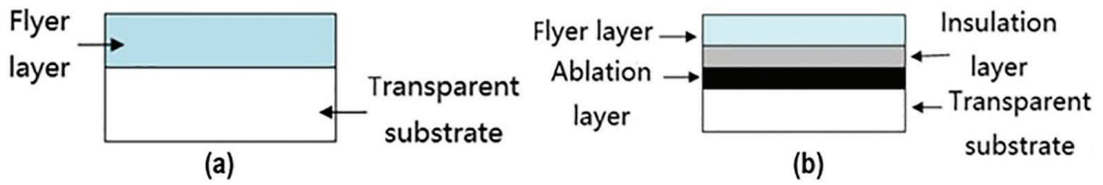

Figure 4. Structure of (a) single-layer flyer and (b) multilayer flyer.

Multilayer flyer is developed according to the formation process of laser-driven flyer. Generally, multilayer flyer owns three-layer structure, as shown in **Figure 4(b)**. The main function of ablation layer is to absorb laser energy and be ablated to form plasma with high temperature and high pressure to drive the flyer. Thermal insulation layer is to restrain the formation and diffusion of plasma in order to reduce the ablation of flyer and ensure its integrity. Sometimes multilayer flyer can be divided into four layers. An absorption layer is added between ablation layer and transparent substrate to improve the absorption of laser energy.

2.1.2. Typical flyer targets

Several typical flyer targets are listed in **Table 1** in detail. In laser-driven flyer impact initiation technology, the research on flyer has been developed from single-metal flyer to multilayer flyer.

According to **Table 1**, the main materials of single-layer flyer are Al and Cu. As for multilayer flyer, the ablation layer materials are mostly C, Al, Mg, Ge, Ti, Zn, etc. Al_2O_3, MgF_2, ZnS, and TiO_2 are commonly good choices for thermal insulation materials. Al, Ti, and Cu are usually used to prepare flyer layers.

2.2. Characteristics of laser-driven flyer

In the study of laser-driven flyer impact initiation technology, the detonation of explosive depends mainly on the impact stress of flyer and pulse width of impact stress. The impact stress of flyer depends on the velocity, structure, and material of flyer while the pulse width

Structure	Author	Flyer layer	Insulation layer	Ablation layer	Absorption layer	Transparent substrate
Single-layer flyer	S. A. Sheffield [3]	Al	—	—	—	—
		Al	—	—	—	BK7
	D. L. Paisley [4]	Al, Cu	—	—	—	glass
Multilayer flyer	D. L. Paisley [5, 6]	Al, Cu	Al_2O_3	—	—	
	D. B. Stahl [7]	Al	—	C	—	
	W. M. Trott [8, 9]	Al	Al_2O_3	Al	—	or
	D. J. Hatt and J. A. Waschl [10]	Al, Cu	Al_2O_3, MgF_2, ZnS	Al, Mg	—	
	J. L. Labaste [11]	Al	Al_2O_3	Ge, C, Ti, Al	—	K9 glass
	D. L. Paisley [12, 13]	Al	Al_2O_3	Al	C	
	M. D. Bowden and S. L. Knowles [14]	Al, Ti	Al_2O_3, TiO_2	C, Mg, Ge, Al, Ti	C, Ti	or
	L. Wu [15]	Al	Al_2O_3	Al	CuO	
	H. R. Brierley [16]	Al	Al_2O_3	Ge, Ti, Zn		Sapphire glass

Table 1. Typical laser-driven flyer targets researched.

of impact stress depends on the planarity and integrity of flyer. Therefore, it is necessary to select flyer with high velocity, strong impact stress, and good planarity and integrity to develop laser-driven flyer impact initiation technology.

2.2.1. Velocity of flyer

2.2.1.1. Measurement of velocity

The velocity of flyers can be measured via photonic Doppler velocimetry (PDV). **Figure 5** shows a schematic view of PDV. It is mainly based upon two physical processes: Doppler effect and optical mixing, that is, heterodyning.

Figure 6 shows schematic view of the measuring setup of flyer velocity. Velocity information of flyer is collected and recorded by PDV measurement system and time history of flyer is obtained by computer program analysis.

2.2.1.2. Regularity of velocity

According to the research of Wu [15] in Nanjing University of Science and Technology, four types of flyers including Al/Al_2O_3/Al multilayer, C/Al/Al_2O_3/Al multilayer, Mg/Al/Al_2O_3/Al multilayer and Al single-layer were tested with the laser energy of 36.4–195.1 mJ by PDV measurement system. The result is indicated in **Figure 7**.

According to **Figure 7**, the analysis to result are as follows. At the same laser energy, Mg/Al/Al_2O_3/Al multilayer flyer owns the maximum velocity, which is little bit better than Al single-layer flyer. The velocity of C/Al/Al_2O_3/Al multilayer flyer is higher than that of Al/Al_2O_3/Al multilayer flyer when the laser energy is less than 150 mJ. Within the range of 150–195.1 mJ of laser energy, the velocity of C/Al/Al_2O_3/Al multilayer flyer is comparable to that of Al/Al_2O_3/Al multilayer flyer. As the ablation layer, Mg layer can greatly improve the velocity of flyer. The addition of Al_2O_3 insulation layer increases the mass of flyer, which makes the velocity

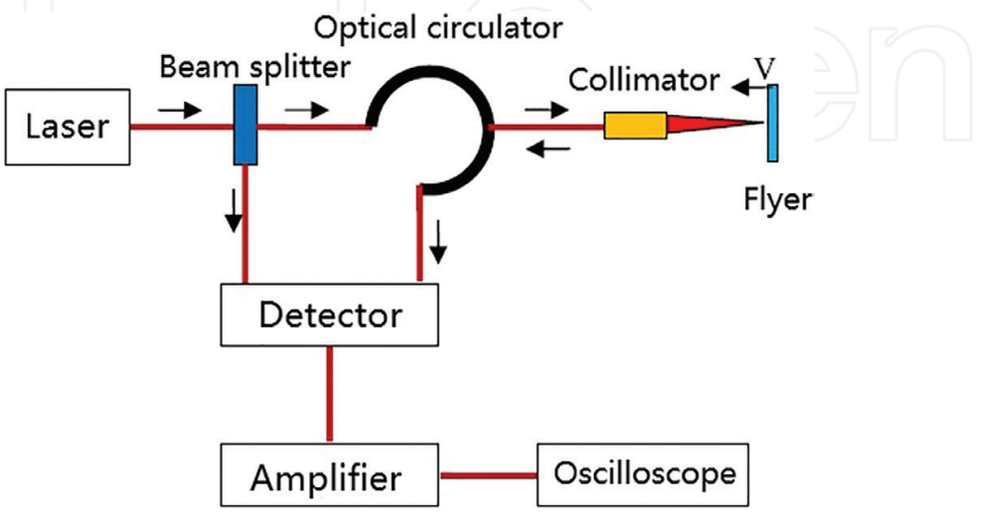

Figure 5. Schematic of PDV.

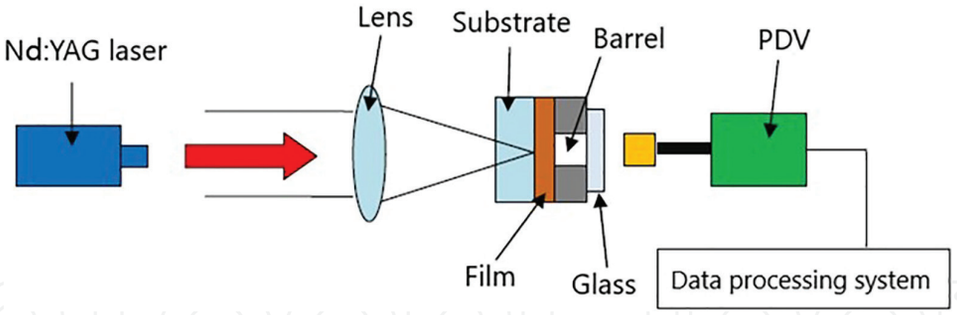

Figure 6. Schematic of measuring setup of flyer velocity.

of $Al/Al_2O_3/Al$ multilayer flyer lower than that of Al single-layer flyer. The addition of C absorption layer increases the velocity of $C/Al/Al_2O_3/Al$ multilayer flyer at low laser energy. However, C layer is easy to be broken down at high laser energy, which reduces the restraining effect of substrate and accelerating chamber to plasma. As a result, the velocity of $C/Al/Al_2O_3/Al$ multilayer flyer is lower than that of $Al/Al_2O_3/Al$ multilayer flyer.

2.2.2. Impact stress of flyer

2.2.2.1. Measurement of impact stress

The impact stress can be measured by a polyvinylidene fluoride (PVDF) pressure sensor (shown in **Figure 8**), and the current mode of PVDF pressure sensor is used to measure the impact stress of flyer.

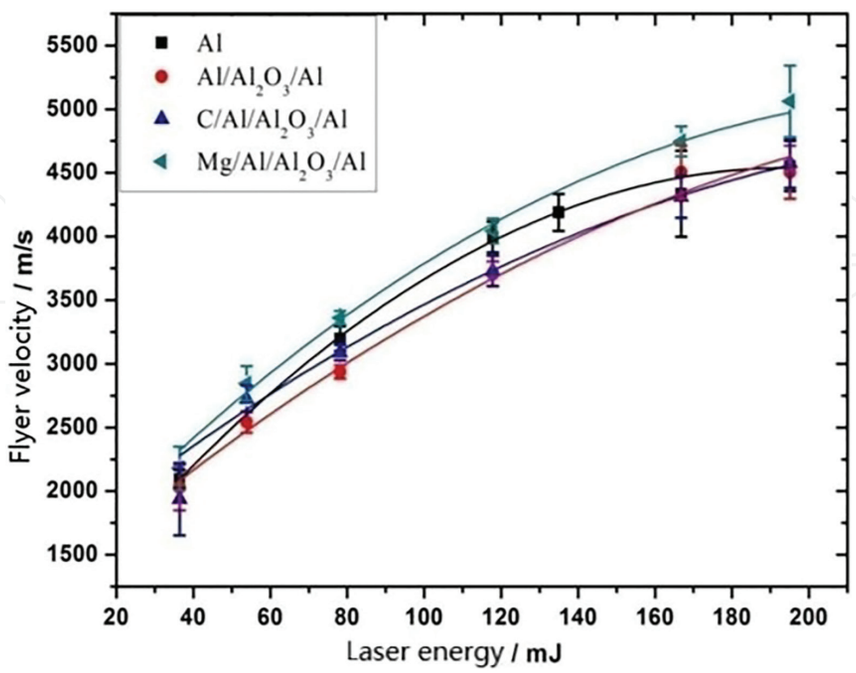

Figure 7. Final velocities of four flyers in different laser energy.

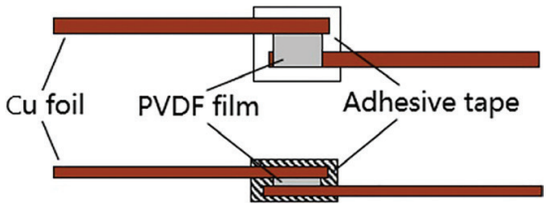

Figure 8. Structure of PVDF sensor.

2.2.2.2. Regularity of impact stress

Figure 9(a) shows the impact stress of six types of flyers at 175, 212, 248, 282, 315, and 362 mJ laser energy, respectively. With the increase of laser energy, the impact stresses of flyer tend to rise up gradually. At the same laser energy, the impact stress of Al single-layer flyer is lower than Al/Al_2O_3/Al multilayer flyer. When the laser energy is not more than 248 mJ, the impact stress of CuO/Al/Al_2O_3/Al multilayer flyer is comparable to that of CuO/Al_2O_3 /Al multilayer flyer. As the energy continues to increase, the impact stress of former will exceed that of the latter. In most cases, the impact stress of C/Mg/Al/Al_2O_3/Al multilayer flyer is greater than C/Al/Al_2O_3/Al multilayer flyer.

In 1969, Walker and Wasley [17] proposed the criterion for impact initiation of heterogeneous explosive

$$E_C = P^2 \tau \tag{2}$$

In Eq. (2), P is the shock wave pressure entering into explosive, τ is the time that shock wave travels back and forth in flyer, and E_c is a constant determined by the specific explosive. Only when the value of $P^2\tau$ is higher than that of E_c, the explosive can be initiated. Ignoring the area effect of impact initiation, the criterion for it can be written as

$$P^2 \tau \geq E_C \tag{3}$$

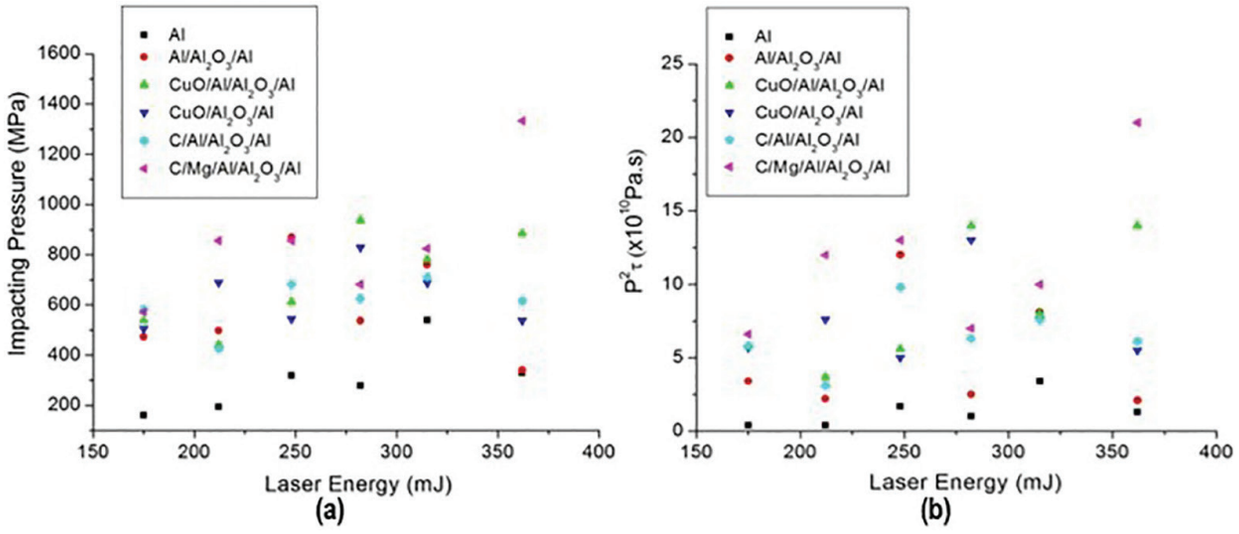

Figure 9. Impact stresses (a) and value of $P^2\tau$ for flyers at different laser energy (b).

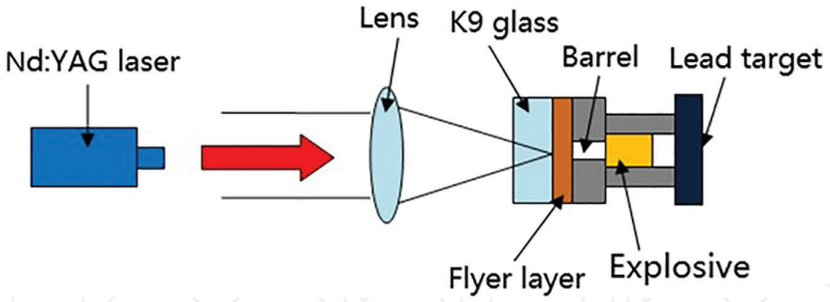

Figure 10. Schematic view of measuring setup for impact initiation.

Value of $P^2\tau$ for six types of flyers are shown in **Figure 9(b)**. The value of $P^2\tau$ indicates the flyer's ability to initiate explosive. It is obvious from **Figure 10** that $P^2\tau$ of multilayer flyers is higher than that of single-layer flyers. Especially, C/Mg/Al/Al_2O_3/Al multilayer flyer obtains the maximum value of $P^2\tau$, which means the best ability to initiate explosive.

2.3. Characteristics of laser-driven flyer impact initiation

2.3.1. Theory of initiating explosives

Impact initiation of agglomerate explosive is a significant initiation method besides thermal initiation. Due to the press fitting of solid agglomerate explosive, voids are retained around the crystal grains with the degree of porosity of 1–4%. After the shock wave entering explosive, the air voids and bubbles are compressed adiabatically under impact. The specific heat of gas is lower than that of the explosive crystal. Therefore, the temperature of bubble is higher than that of the crystal, which will cause the appearance of hot spots.

2.3.2. Measuring setup for impact initiation

The schematic view of measuring setup for impact initiation is shown in **Figure 10**. The laser focused by lens irradiates on flyer target and ablates a part of the film to form plasma. Immediately, the remaining part of the film is sheared along the edge of accelerating chamber and is driven out at high velocity to form a flyer. Then, the flyer is accelerated in accelerating chamber and hits explosive cylinder causing the explosive to be struck and detonated.

2.3.3. Initiation of PETN

Five types of flyers including Al and Cu single-layer flyers and CuO/Cu, CuO/Al and CuO/Al/Cu multilayer flyers with relatively high velocities were used to initiate PETN explosive [15]. The results are shown in **Table 2**.

Compared to the results in **Table 2**, it is easy to find that Al single-layer flyer shows the best performance of initiation in the same laser energies, which succeeded in initiating as long as the laser energy was higher than 161 mJ. CuO/Cu multilayer flyer owned four successful detonations as well. Besides, the success rate of initiation for other flyers is arranged from high to low, followed by Cu single-layer flyer, CuO/Al and CuO/Al/Cu multilayer flyers. The results indicate

Structure of flyer	Laser energy/mJ	67	109	161	203	264	336.7	375.7
Cu	Flyer velocity/m·s^{-1}	1965	2402	2597	3389	3389	4020	3065
	$P^2\tau$/×10^{10} Pa·s	0.2	0.2	1.3	6.3	10.4	6.3	3.0
	Detonation	×	×	×	√	√	√	×
Al	Flyer velocity/m·s^{-1}	3162	3433	4145	4324	4761	5194	5000
	$P^2\tau$/×10^{10} Pa·s	0.2	0.9	5.4	5.6	9.4	7.6	6.6
	Detonation	×	×	√	√	√	√	√
CuO/Cu	Flyer velocity/m·s^{-1}	2105	2500	2649	2909	3149	3252	3305
	$P^2\tau$/×10^{10} Pa·s	2.1	1.5	2.6	5.8	6.8	5.4	7.1
	Detonation	×	×	×	√	√	√	√
CuO/Al	Flyer velocity/m·s^{-1}	3478	3773	4597	4878	5031	4848	5673
	$P^2\tau$/×10^{10} Pa·s	0.6	2.4	3.2	3.7	11.0	8.7	4.9
	Detonation	×	×	×	×	√	√	×
CuO/Al/Cu	Flyer velocity/m·s^{-1}	2352	2507	2702	3100	3265	3791	3625
	$P^2\tau$/×10^{10} Pa·s	0.9	1.1	1.9	3.3	5.1	2.0	2.0
	Detonation	×	×	×	×	√	×	×

Table 2. Initiation results of PETN for different types of flyers.

that a certain range of laser energy is necessary in the process of laser-driven flyer impact initiation, which can ensure enough velocity and impact stress of flyer.

2.4. Analysis of laser-driven flyer initiating explosives

There are two main factors affecting the impact initiation of flyer including velocity and shape of flyer, which are indispensable. Al flyer shows the best performance in impact initiation while CuO/Al and CuO/Al/CuO multilayer flyers show the worst performance. It is analyzed that the oxidation reaction between Al and CuO will release a lot of energy to melt or vaporize some part of flyer and change the shape of flyer, which can reduce the impact effect of it and result in the decrease of flyer velocity. The velocity of Cu flyer is higher than Al's, but its impact initiation ability is not as good as Al flyer. This is because Cu flyer is more brittle than Al flyer and is more likely to be broken during flight, which will affect the initiation effect. A large number of experimental results show that a certain range of laser energy is needed to drive the flyer. Thus, the velocity and impact stress can be high enough to initiate the explosives successfully.

3. Laser-induced time of flight mass spectroscopy of typical energetic materials

Laser-material interaction is essentially based on thermal and photonic processes, where as a consequence of laser irradiation, different phenomena occur on a microscopic or macroscopic scale [18]. It will populate an excited state that can either couple to a reaction pathway, resulting

in chemical reactions, or undergo internal conversion back to the ground state of the starting molecule. A microscopic understanding of the complex physical and chemical processes involved in the combustion and decomposition of energetic material is essential for the development of predictive detonation and reliable model for performance, stability, and hazard analysis of explosives [19]. Many investigations have been conducted concerning the mechanism of decomposition of explosives under laser irradiation [20–22].

In order to ensure the reliability and safety of laser initiation system, it is necessary to reveal the microscopic mechanism of the reaction of energetic materials under laser irradiation. Spectroscopic method is an effective means to reveal the mechanism of laser-induced dissociation of energetic materials [23]. In the present work, time of flight mass spectrometry (TOFMS) was employed to study the ion fragments produced by explosives after laser excitation with the purpose of understanding the effect of different experimental parameters on the resultant mass spectra and laser-induced reaction.

3.1. Detection of laser-induced decomposition products

The explosive samples were pressed into an aluminum holder (6 mm diameter and 11 mm depth) using a pressing tool to ensure a flat surface and a consistent filling density with a pressure of 80 MPa. The apparatus used in this study was a homemade reflection time of flight mass spectrometer. The time of flight mass spectrometer consists of four parts: ion source, ion acceleration zone, flight area, reflector and detector. The detector is made from a pair of microchannel plates (MCPs) [24]. It was combined with a vacuum chamber, pumping down to 4×10^{-4} Pa with two turbomolecular pumps. The output from a Q-switched Nd:YAG laser (LOTIS TII, LS-2147, 450 mJ@532 nm/15 ns, 800 mJ@ 1064 nm/15 ns) was focused to the sample surface by a quartz focus lens with focus length of 500 mm) and spot size of about 0.8 mm^2. The laser fluence was measured by an energy meter (Ophir, Model 30A). After ionization, the laser generated ion fragments were first driven by the initial kinetic energy into the acceleration zone, and then accelerated by a pulsed electric field, and finally detected by the MCPs [25]. The ions were mass analyzed by its flight time. In order to reduce the noise, the weak signal measurement technique with multiple signal superposition was adopted. The TOF signals were accumulated 128 times by a digital oscilloscope (Tektronix, DPO7140) to improve the signal-to-noise ratio. The trigger of each instrument was controlled by a pulse delay generator (University of Science and Technology of China, GH024). **Figure 11** shows the schematic diagram of the experimental setup [18].

3.2. Laser-induced TOF mass spectroscopy of nitramines

3.2.1. RDX

Typical negative and positive ion mass spectra of RDX obtained by 532 nm laser dissociation are shown in **Figure 12**. The laser energy was 4.8 J/cm^2 for negative ions with delay time of 50 μs and 5.2 J/cm^2 for positive ions with delay time of 50 μs. For negative mode, the peak with the highest intensity in the negative-ion spectrum are at m/z = 46 and corresponds to the NO_2 fragment. Other relatively strong peaks appear at m/e = 26, 106, and 134 and can be assigned to CN, $(CNC)C(NN)_{2,}$ and $H_2C(N\text{-}NO_2)_2$, respectively. Finally, some low intensity

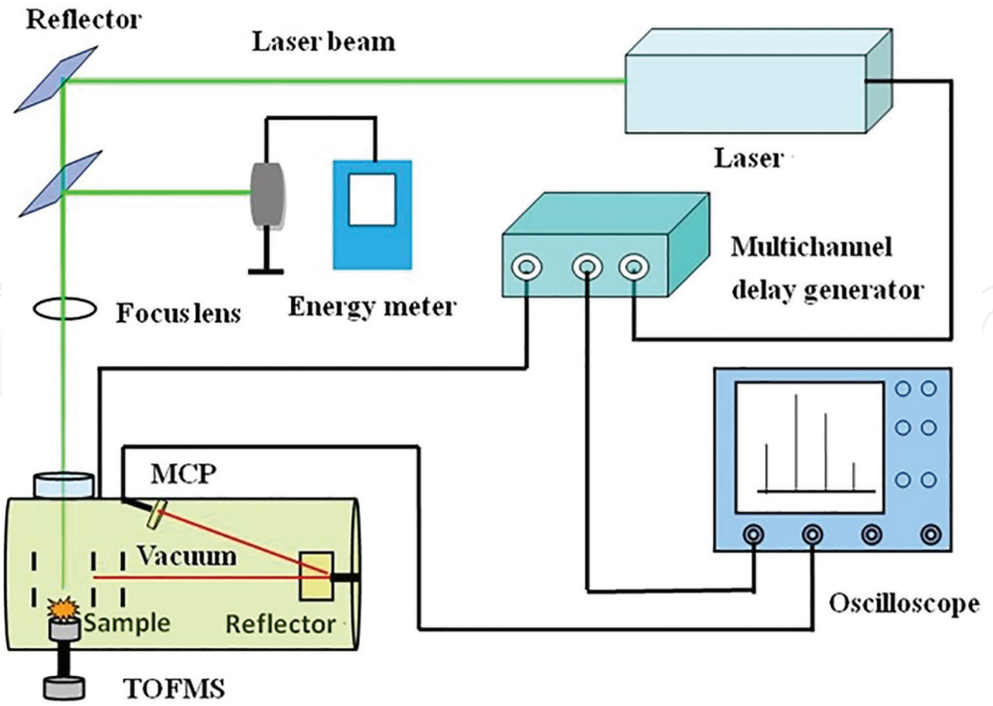

Figure 11. Schematic diagram of the TOFMS system.

peaks are observed at m/z = 42,60,84,88,93,130, and 176, possible assignments for major peaks are $N(CH_2)N$, $N\text{-}NO_2$, $(H_2CN)_3$,$(CH_2)_2N\text{–}NO_2$, (CH)(NCNC)(NN), $(CH_2)_3N(N\text{-}NO_2)N$ and $(CH_2)_3(N\text{-}NO_2)_2N$, respectively. For positive mode, positive ions have three series, m/z = 17 can be attributed to OH. m/z = 26, 27, 28, 29, 30, and 32 ions can be classified as CN, HCN, $CO/N_2/H_2CN$, HCO, NO, and O_2, respectively. The third series with m/z of 42, 44, and 47, and their corresponding attributions are C_2H4N/ CH_2N_2/N (H_2C) N, N_2O/CH_2NO, and HONO, respectively [18, 26].

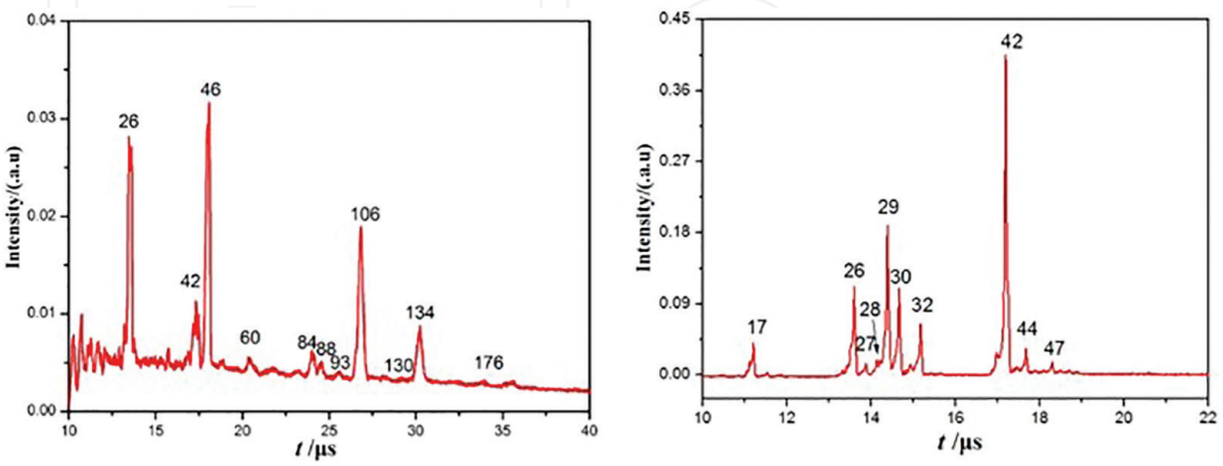

Figure 12. Typical TOF mass spectra of negative ions (left) and positive ions (right) for RDX produced by 532 nm laser ablation.

Typical negative and positive ion mass spectra of RDX obtained by 1064 nm laser dissociation are shown in **Figure 13**. The laser energy was 34.9 J/cm^2 for negative ions with delay time of 80 μs and 49.4 J/cm^2 for positive ions with delay time of 70 μs. The position of the peaks of negative ion mass spectrum under 1064 nm is similar to that under 532 nm. The difference lies in the intensity of the major peak. From the negative ions mass spectrum, it can be found that the highest peak with the appears at m/z = 106 and corresponds to $CH_2(NO_2)_2$ fragment. Different with the results at 532 nm, two small new peaks produce at m/z = 98 and 100, which can be assigned to $(CH_2)_3N_2(NN)$ and $(CH_2)_3N_2(NO)$. The relative strong peaks at m/z = 26, 46, 88 and 134 may be CN or C_2H_2, NO_2, $(CH_2)NNO_2$, and $H_2C(N\text{-}NO_2)_2$. Moreover, the peaks with low intensity can be observed at m/z = 42, 64, and 84 are most likely the CNO or $(CH_2)_2N$ or CH_2N_2 and $(CH_2N)_3$ fragments, respectively. In the positive ions mass spectrum, the peak with the highest intensity can be found at m/z = 30, corresponding to the NO or CH_2O species. The second strong peak appears at m/z = 18, and can be ascribed to H_2O or NH_4, respectively. A series of peaks are observed at m/z = 40, 42, 43, 44, 46, and 47, and can be ascribed to CN_2 or C_2H_2N, $N(CH_2)N$ or $(CH_2)_2N$, NCOH, N_2O or CO_2 or CH_2NO, NO_2 and HONO, respectively. The thermal decomposition results of the isotopically labeled RDX confirmed that the formula for the ion signal at m/z = 45 was H_2NCHO and which might be formamide. Likewise, the isotopically labeled results also showed that m/z = 59 was corresponding to CH_3NHCHO and was most likely N-methylformamide. Some small peaks can be observed at m/z = 57, 58, 59, and 60, these ions can be assigned to $(CO)NH(CH_2)$ or N(COH)N, CNO_2 or $(COH)NH(CH_2)$, $CHNO_2$ and CH_2NO_2, or NNO_2, respectively. Some other peaks can be found at m/z = 16, 19, 24, 27, 28, 74, 79, and 86, which may be from CH_4 or O, H_3O, C_2, C_2H_3, or CHN, N_2 or CO or C_2H_4 or CH_2N, CH_2NNO_2, $(HC)N(CN)_2$, and $(CH)_2NNO_2$, respectively [18, 25].

3.2.2. HMX

Typical negative and positive ion mass spectra of HMX obtained by 532 nm laser dissociation are shown in **Figure 14**. The laser energy was 8.6 J/cm^2 for negative ions with delay time of 75 μs and 7.8 J/cm^2 for positive ions with delay time of 70 μs. It can be seen from the negative

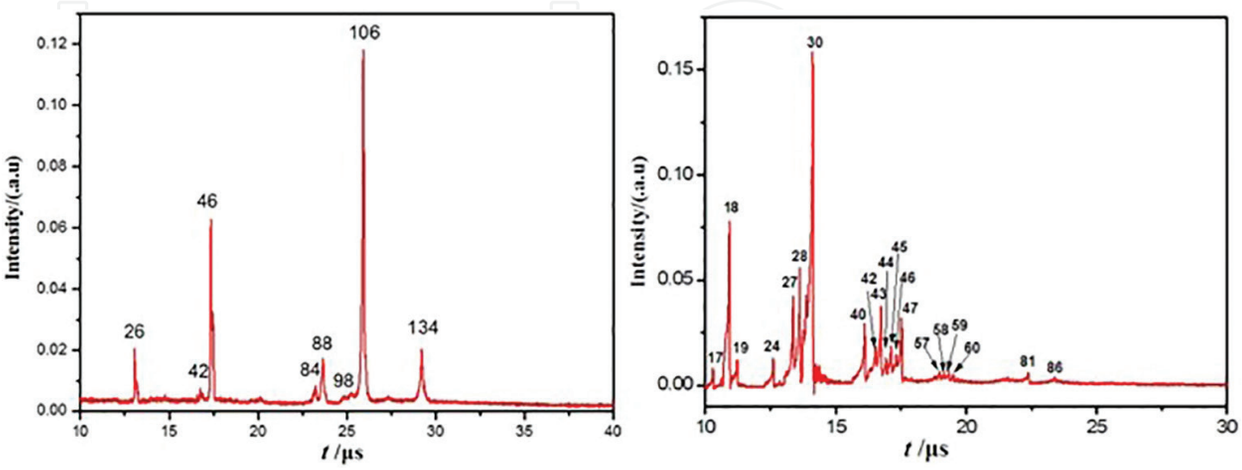

Figure 13. Typical TOF mass spectra of negative ions (left) and positive ions (right) for RDX produced by 1064 nm laser ablation.

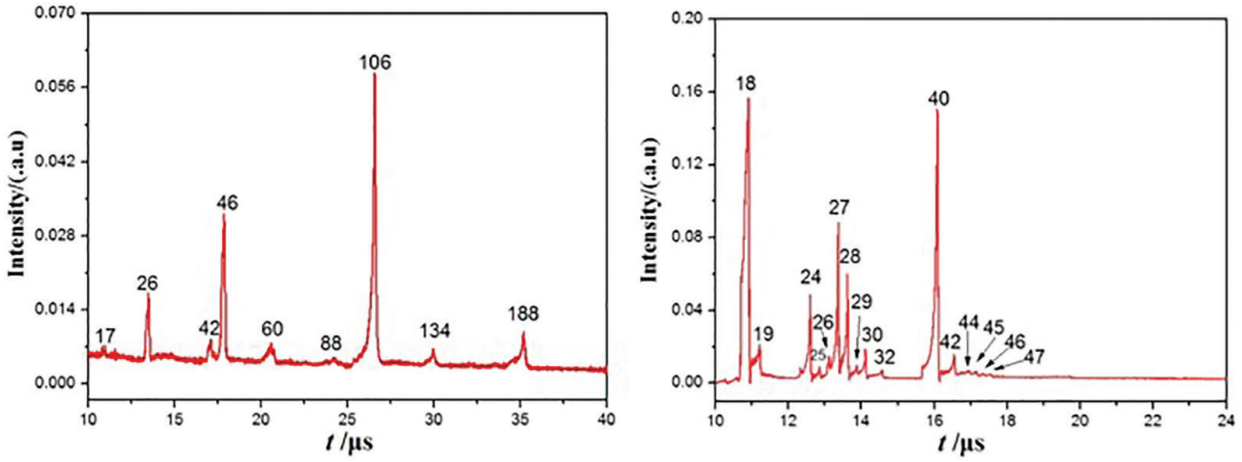

Figure 14. Typical TOF mass spectra of negative ions (left) and positive ions (right) for HMX produced by 532 nm laser ablation.

ion spectrum that the ion distribution of HMX has some similarity with that of RDX. HMX has three strong ion peaks with *m*/*z* of 26, 46, and 106. According to the molecular structure and decomposition properties of HMX, it can be deduced that these three peaks are CN_2 and $NO_2(NO_2)_2/N(NO_2)_2$, respectively. There are some relatively weak peaks at *m*/*z* of 17, 42, 60, 88, 134, and 188, which correspond to OH, $CH_2N_2/C_2H_2O/CNO$, CH_2NO_2/N_2O_2, $(CH_2)_2NNO_2$, $CH_2(NNO_2)_2$, and $CNN(CH_2NNO_2)_2$, respectively. The distribution of positive ions is obviously different from that of negative ions, which is mainly distributed in three regions: *m*/*z* of 18 and 19 were in the first region, which may be due to H_2O and H_3O, respectively. The *m*/*z* of the second distribution region is 24–32, the possible attributions are C_2(*m*/*z* = 24), C_2H(*m*/*z* = 25), CN(*m*/*z* = 26), HCN(*m*/*z* = 27), $CO/N_2/H_2CN$ (*m*/*z* = 28), HCO (*m*/*z* = 29), NO/CH_2O (*m*/*z* = 30), and O_2 (*m*/*z* = 32). The *m*/*z* of the third distribution region is 40–47, which can be assigned to CN_2/C_2H_2N (*m*/*z* = 40), $CH_2N_2/C_2H_2O/CNO$ (*m*/*z* = 42), $N_2O/CO_2/CH_2NO$(*m*/*z* = 44), HN_2O (*m*/*z* = 45), NO_2 (*m*/*z* = 46), and HONO (*m*/*z* = 47), respectively [18].

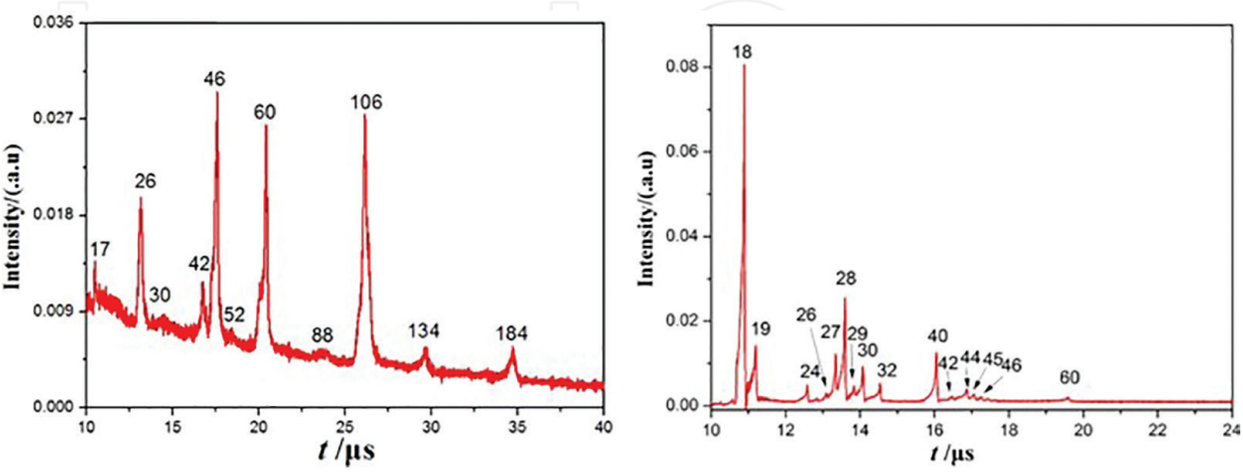

Figure 15. Typical TOF mass spectra of negative ions (left) and positive ions (right) for HMX produced by 1064 nm laser ablation.

Typical negative and positive ion mass spectra of HMX obtained by 1064 nm laser dissociation are shown in **Figure 15**. The laser energy was 45.0 J/cm^2 for negative ions with delay time of 80 μs and 41.4 J/cm^2 for positive ions with delay time of 70 μs. The distribution of negative ion peaks of HMX at 1064 nm is similar to that of 532 nm laser, and all of them have more obvious ion peaks at *m*/*z* of 17(OH), 26(CN), 42 (CH_2N_2/C_2H_2O/CNO), 46(NO_2), 60(CH_2NO_2/N_2O_2), 88(($CH_2)_2NNO_2$), 106 ($N(NO_2)_2$/$CH_2(NO_2)_2$), and 134 ($CH_2(NNO_2)_2$), except that the relative intensity of *m*/*z* of 60 and 46 increased significantly and a new ion peak $CNN(CNNO_2)_2$ is generated at *m*/*z* of 184. The distribution of positive ions is almost the same as that of 532 nm. However, there are differences in the intensity for the ions, among which the relative intensity of 24 (C_2), 27(HCN), and 40(CN_2/C_2H_2N) reduced significantly. The similarity of the distribution of ions indicates that the decomposition mechanism of HMX under the irradiation of two kinds of laser wavelengths is similar [18, 24].

3.3. Laser-induced TOF mass spectroscopy of aromatic nitro compounds

3.3.1. TNT

Typical negative and positive ion mass spectra of TNT obtained by 532 nm laser dissociation are shown in **Figure 16**. The laser energy was 24.6 J/cm^2 for negative ions with delay time of 70 μs and 25.8 J/cm^2 for positive ions with delay time of 70 μs. For the negative ions, the strongest peak appeared at *m*/*z* = 26, which might correspond to CN. Two relatively strong peaks appeared at *m*/*z* = 42 and 46, which might be due to CH_2N_2/C_2H_2O/CNO and NO_2. A series of small peaks were observed at *m*/*z* = 50, 66, 77, 137, 152, 167, 197, 212, 225, and 238, these ions could be ascribed to CHCCHC, CCHCOCH, CHCHCHCHCHC, $CH_3CHCOCHCOCCO$, $(CHCO)_2CCNO_2$, $CH_3(CHCO)_2CCNO_2$, $CH_3CHCOCHCNO_2CCNO_2$, $C_6H_2(NO_2)_3$, $C_6H_2CH(NO_2)_3$, and $C_6H_2CHCH(NO_2)_3$. The mass charge ratio of $C_6H_2CHCH(NO_2)_3$ (*m*/*z* = 238) is larger than TNT (*m*/*z* = 227), it can be conjectured that TNT may get some atoms to form larger fragments. For the positive ions, the dominant peaks were appeared at *m*/*z* = 18, 19, 24, 27, 28, 30, and 40, these ions could be correspond to H_2O, H_3O, C_2, HCN, CO/N_2/CH_2N, NO,

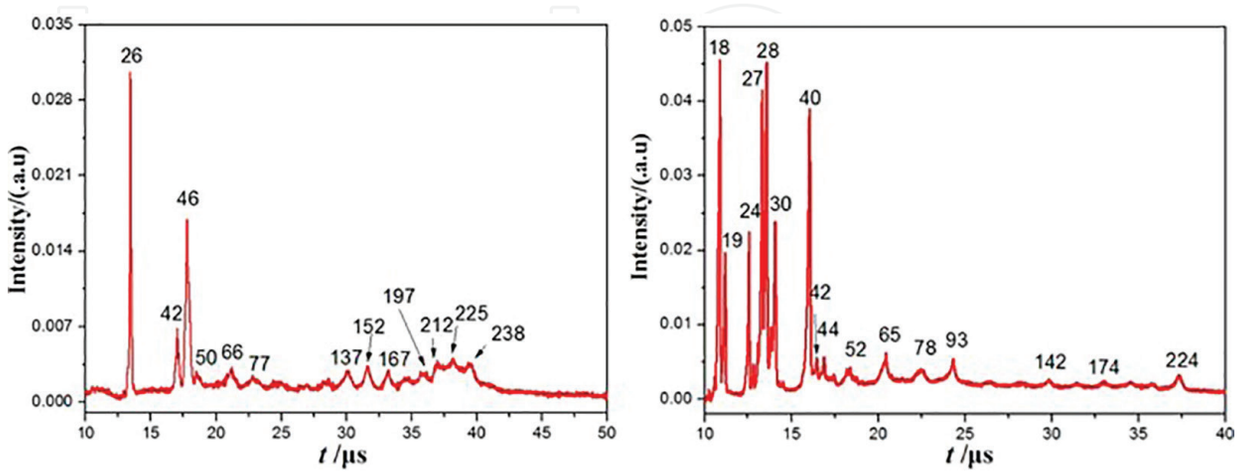

Figure 16. Typical TOF mass spectra of negative ions (left) and positive ions (right) for TNT produced by 532 nm laser ablation.

and C_2H_2N. Some low intensity peaks were observed at 42, 44, 52, 65, 78, 93, 142, 174, and 224, possible assignments for these peaks were $CH_2N_2/C_2H_2O/CNO$, $N_2O/CO_2/CH_2NO$, C_2N_2, CNCHCN, C_6H_6, C_6H_5O, $(CCN)_2C$ (CCNO), $C(CCNO)_3$, and $C(CHNO_2)_2(CCNO_2)$ [18, 27].

Typical negative and positive ion mass spectra of TNT obtained by 1064 nm laser dissociation are shown in **Figure 17**. The laser energy was 15.9 J/cm^2 for negative ions with delay time of 70 μs and 13.3 J/cm^2 for positive ions with delay time of 70 μs. Compared with previous studies at 532 nm laser irradiation, we find that the distribution of both the negative and positive ion fragments has a certain similarity. The difference is that three strong peaks appear at m/z = 26, 212, and 238 for the negative ion mode after 1064 nm irradiation, which can be attributed to CN, $C_6H_2(NO_2)_3$, and $C_6H_2(NO_2)_3(CHCH)$, as shown in **Figure 3**. At the same time, some weak negative ion fragment peaks are produced at m/z = 92, 103, 116, 146, 158, 176, and 197, these peaks are probably attributable to $(CCH)_2(CHCOH)$, $(CCH)_2CO(CCH)$, $(CCO)_2C_3$, $(CCO)_2C(CCON)$, $(CCON)_2CC(CN)$, $(CCON)(CCNO_2)$ C(CCO), and $CH_3(CHCO)$ $(CHCNO_2)$ $CCNO_2$. For the positive ion mode, different with 532 nm, these peaks at m/z = 24, 27, 30, 40, 42, 65, 78, 93, and 174 are observed, these ion fragments may be due to C_2, HCN, NO, C_2H_2N, $CH_2N_2/C_2H_2O/CNO$, CNCHCN, C_6H_6, C_6H_5O, and $C(CCNO)_3$ [18, 28].

3.3.2. HNS

Typical negative and positive ion mass spectra of HNS obtained by 532 nm laser dissociation are shown in **Figure 18**. The laser energy was 8.6 J/cm^2 for negative ions with delay time of 60 μs and 8.6 J/cm^2 for positive ions with delay time of 55 μs. For the negative mode, the main peaks appear at m/z = 26, 42, 46, and 62, which corresponds to the CN, $CH_2N_2/C_2H_2O/CNO$, NO_2, and NO_3 fragments. A series of relatively weak peaks can be found at m/z = 50, 66, 77, 93, 107, 142, 172, 196, 212, 225, and 238. According to the structure of HNS, these peaks can be assigned to $(CHC)_2$, CCHCOCH, C_6H_5, C_6H_5O, C_6H_5NO, $(CCN)_2C(CCNO)$, $(CCN)_2CNO$ (CCNO), $C_6H_2NO(NO_2)_2$, $C_6H_2(NO_2)_3$, $C_6H_2CH(NO_2)_3$, and C_6H_2CHCH $(NO_2)_3$, respectively. For the positive mode, the peaks with high intensity are mainly distributed in m/z = 28, 30,

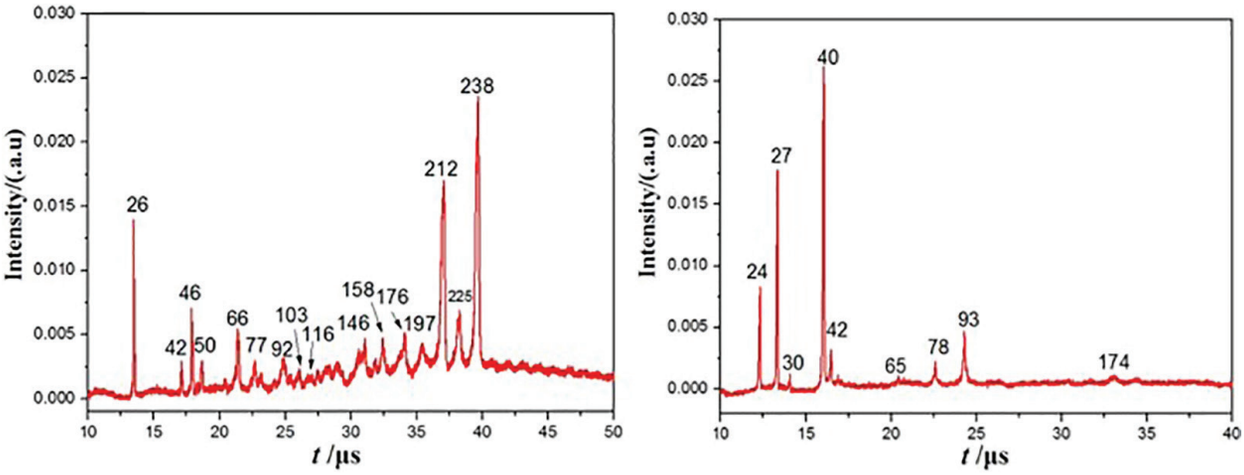

Figure 17. Typical TOF mass spectra of negative ions (left) and positive ions (right) for TNT produced by 1064 nm laser ablation.

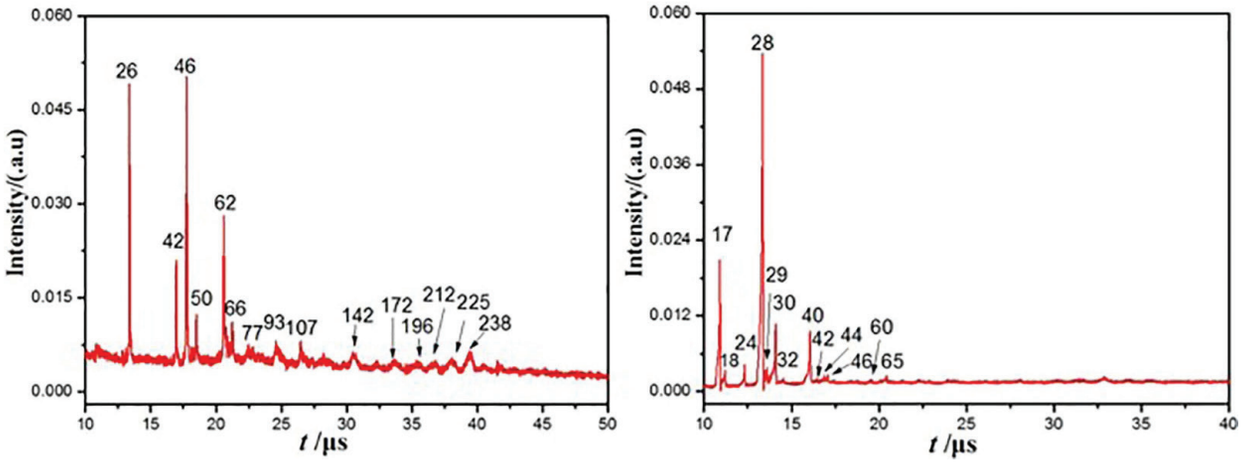

Figure 18. Typical TOF mass spectra of negative ions (left) and positive ions (right) for HNS produced by 532 nm laser ablation.

17, and 40, respectively, corresponding to OH, $CO/N_2/CH_2N$, NO, and CH_2CN. In addition, at m/z = 18, 24, 29, 32, 42, 44, and 65, the strength of the ions is weak, which can be attributed to H_2O, C_2, CHO, O_2, $CH_2N_2/C_2H_2O/CNO$, $N_2O/CO_2/CH_2NO$, and CNCHCN, respectively [18].

Typical negative and positive ion mass spectra of HNS obtained by 1064 nm laser dissociation are shown in **Figure 19**. The laser energy was 8.4 J/cm^2 for negative ions with delay time of 80 μs and 13.1 J/cm^2 for positive ions with delay time of 70 μs. For the negative ions, a strong peak is observed at m/z = 26, which can be attributed to CN fragment. A series of regular peaks with a mass to charge ratio step of 4 appear at m/z = 42, 46, and 50, according to the molecular structure of HNS, possible assignments for these peaks are $CH_2N_2/C_2H_2O/CNO$, NO_2, and CHCCHC. Fragments like CH_2N_2, C_2H_2O, and CNO that have similar mass to charge ratio are difficult to distinguish from the instrument due to the limited mass resolution, which mainly caused by the large broadening of the kinetic energy distributions of the species produced in the excitation process. Another series

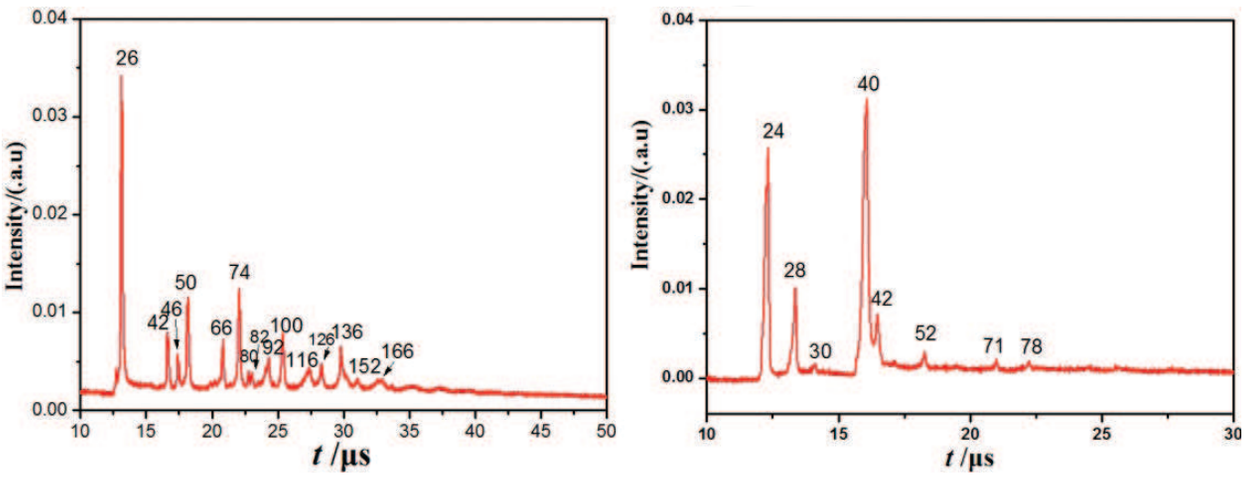

Figure 19. Typical TOF mass spectra of negative ions (left) and positive ions (right) for HNS produced by 1064 nm laser ablation.

of peaks can be found at m/z = 50, 66, 74, 80, 82, 92, 100, 116, 126, 136, 152, and 166, these peaks can be assigned to CHCCHC, CCHCOCH, C_6H_2, CHCCHCNO, CHNCHCNO, CHCCHCCNO, C_6H_2CN, C_6H_2CNO, $CHCNOCHCNO_2$, $C_6H_2ONO_2$, $C_6H_2O_2NO_2$, and $C_6H_2ONONO_2$, respectively. Unlike the spectra in the positive mode, there are less ion lines in the negative mode. The dominant peaks appear at m/z = 24, 28, 40, and 42, which corresponded to C_2, $CO/N_2/CH_2N$, CH_2CN, and $CH_2N_2/C_2H_2O/CNO$, respectively. Some relatively weak peaks can be found at m/z = 30, 52, 71, and 78, which may be due to $(CN)_2$/CHCNCH, $CHCNO_2$, and C_6H_2N, respectively [18, 29].

4. Conclusions

The structure of flyer target can be divided into two types: single-layer flyer and multilayer flyer. The main materials of single-layer flyer are Al and Cu. As for multilayer flyer, the ablation layer materials are mostly C, Al, Mg, Ge, Ti, Zn, etc. Al_2O_3, MgF_2, ZnS, and TiO_2 are commonly good choices for thermal insulation materials. Al, Ti, and Cu are usually used to prepare flyer layers. Four types of flyers including $Al/Al_2O_3/Al$ multilayer, $C/Al/Al_2O_3/Al$ multilayer, $Mg/Al/Al_2O_3/Al$ multilayer, and Al single-layer were tested with the laser energy of 36.4–195.1 mJ by PDV measurement system. At the same laser energy, $Mg/Al/Al_2O_3/Al$ multilayer flyer owns the maximum velocity. Mg layer can greatly improve the velocity of flyer as the ablation layer. The addition of Al_2O_3 insulation layer increases the mass of flyer, which makes the velocity of $Al/Al_2O_3/Al$ multilayer flyer is lower than that of Al single-layer flyer. The addition of C absorption layer increases the velocity of $C/Al/Al_2O_3/Al$ multilayer flyer at low laser energy. The current mode of PVDF pressure sensor was used to measure the impact stress of flyer. With the increase of laser energy, the impact stresses of flyer tend to rise up gradually. $P^2\tau$ of multilayer flyers are higher than that of single-layer flyers. Especially, $C/Mg/Al/Al_2O_3/Al$ multilayer flyer obtains the maximum value of $P^2\tau$, which means the best ability to initiate explosive. Besides, five types of flyers including Al and Cu single-layer flyers and CuO/Cu, CuO/Al and CuO/Al/Cu multilayer flyers with relatively high velocities were used to initiate PETN explosive. Al single-layer flyer shows the best performance of initiation in the same laser energies, which succeeded in initiating as long as the laser energy was higher than 161 mJ. A certain range of laser energy is necessary in the process of laser-driven flyer impact initiation, which can ensure enough velocity and impact stress of flyer.

Laser ionization time of flight mass spectrometry has been applied to study the decomposition process of typical energetic materials (RDX, HMX, TNT, and HNS). Both the negative and positive ion fragments of these energetic compounds were detected. Based on the structure of explosives, possible attributions of the ion fragments were obtained. The attribution of the ions was similar for the same explosive at two different wavelengths, it indicated that the similar dissociation paths involved in the processes of explosives after irradiated by 532 and 1064 nm laser. For the same category of energetic compounds, the attribution of the ions was similar, that means the dissociation paths were similar. The results might give some help for the further understanding of the process of laser initiation of explosives.

Acknowledgements

This work was supported by the National Natural Science Foundation of China (No. 11604149).

Author details

Ruiqi Shen*, Lizhi Wu, Wei Zhang and Haonan Zhang

*Address all correspondence to: rqshen@njust.edu.cn

Department of Applied Chemistry, School of Chemical Engineering, Nanjing University of Science and Technology, Nanjing, China

References

[1] Goujon J, Musset O, Marchand A, Bigot C. Synchronous initiation of optical detonators by Q-switched solid laser sources. Proceedings of SPIE. 2008;**7115**:71150P-71150P-11

[2] Paisley D, Swift D, Tierney IV T, Munson C, Johnson R. Diagnostics for confined plasma ablation for plate launch and shock generation. Proceedings of SPIE. 2005;**5580**: 868-872

[3] Sheffield S, Rogers J Jr, Castaneda J. Velocity measurements of laser-driven flyers backed by high impedance windows. Shock Waves in Condensed Matter. 1986;541-546. https://link.springer.com/chapter/10.1007/978-1-4613-2207-8_78#citeas

[4] Paisley DL, Montoya NI, Stahl DB, Garcia IA. Interferometry and High Speed Photography of Laser-Driven Flyer Plates. 33rd Annual Techincal Symposium. 1990;245-249

[5] Paisley D. Laser-Driven Miniature Flyer Plates for Shock Initiation of Secondary Explosives, APS Meeting. 1989;14-17

[6] Paisley D. Laser-Driven Flyer Plate. US Patent. US 5046423;1991

[7] Stahl DB, Paisley DL. Carbon-Assisted Flyer Plates, US Patent. US 5301612;1994

[8] Trott WM. Investigation of the Dynamic Behavior of Laser-Driven Flyers. AIP Conference Proceedings. 1994;**309**(1):1655-1658

[9] Trott WM. High-speed optical studies of the driving plasma in laser acceleration of flyer plates. AIP Conference Proceedings. 1996;**370**(1):921-924

[10] Hatt D, Waschl J. A Study of Laser-Driven Flyer Plates. AIP Conference Proceedings. 1996;**370**(1):1221-1224

[11] Labaste JL, Brisset D, Doucet M. Investigation of driving plasma materials for laser acceleration of flyer plates. AIP Conference Proceedings. 2000;**505**(1):1189-1192

[12] Paisley DL. Confined plasma ablation for shock physics, plate launch and material dynamics. High-Power Laser Ablation VI. 2006;**6261**:62611Y

[13] Paisley DL, Luo SN, Greenfield SR, Koskelo AC. Laser-launched flyer plate and confined laser ablation for shock wave loading: Validation and applications. Review of Scientific Instruments. 2008;**79**(2):023902

[14] Bowden M, Knowles S. Optimisation of laser-driven flyer velocity using photonic Doppler velocimetry. Proceedings of SPIE. 2009;**7434**

[15] Wu L. Shock Initiation Technology of Explosives by Laser-Driven Metal Flyer. Nanjing University of Science & Technology; 2010

[16] Brierley H, Williamson DM, Vine T. Improving laser-driven flyer efficiency with high Absorptance layers. AIP Conf. Proc. 2012;**1426**(1):315-318

[17] Walker F, Wasley R. Critical energy for shock initiation of heterogeneous explosives. Explosive Stoffe. 1969;**1**:9-13

[18] Zhang W. Laser-Induced Decomposition Mechanism of Typical Energetic Compounds. Nanjing University of Science & Technology; 2014

[19] Glascoe EA, Zaug JM, Armstrong MR, Crowhurst JC, Grant CD, Fried LE. Nanosecond time-resolved and steady-state infrared studies of photoinduced decomposition of Tatb at ambient and elevated pressure. The Journal of Physical Chemistry A. 2009;**113**(20): 5881-5887

[20] Kosmidis C, Ledingham K, Kilic H, McCanny T, Singhal R, Langley A, Shaikh W. On the fragmentation of nitrobenzene and nitrotoluenes induced by a femtosecond laser at 375 nm. The Journal of Physical Chemistry A. 1997;**101**(12):2264-2270

[21] Civiš M, Civiš S, Sovová Kn, Dryahina K, Španěl P, Kyncl M. Laser ablation of FOX-7: Proposed mechanism of decomposition. Analytical Chemistry. 2011;**83**(3):1069-1077

[22] Delgado T, Alcántara JF, Vadillo JM, Laserna JJ. Condensed-phase laser ionization time-of-flight mass spectrometry of highly energetic nitro-aromatic compounds. Rapid Communications in Mass Spectrometry. 2013;**27**(15):1807-1813

[23] Zhang W, Ma X, Shen R, Wu L, Ye Y, Hu Y, Zhu P. Progress on laser-induced decomposition of explosives investigated by spectroscopic methods. Applied Spectroscopy Reviews. 2014;**49**(7):550-563

[24] Zhang W, Shen R, Ye Y, Wu L, Zhu P, Hu Y. Distribution and formation of particles produced by laser ablation of cyclotetramethylene tetranitramine. Laser and Particle Beams. 2017;**35**(3):1-6

[25] Zhang W, Shen R, Ye Y, Wu L, Hu Y, Zhu P. Dissociation of cyclotrimethylenetrinitramine under 1064-nm laser irradiation investigated by time-of-flight mass spectrometer. Spectroscopy Letters. 2014;**47**(8):611-615

[26] Zhang W, Shen R, Wu L, Qin Z, Ye Y, Hu Y, Zhu P. Dissociation of RDX at 532nm laser. Chinese Journal of Explosives & Propellants. 2012;**35**(1):39-42

[27] Zhang W, Shen R, Ye Y, Wu L, Hu Y, Zhu P. Photodissociation of 2, 4, 6-trinitrotoluene with a Nd: YAG laser at 532nm. Proceedings of SPIE. 2015;**9543**:95431A

[28] Zhang W, Shen R, Ye Y, Wu L, Hu Y, Zhu P. Ion fragments of TNT produced by 1064 nm laser dissociation. Journal of Beijing Institute of Technology (English Edition). 2016;**25**(1): 103-106

[29] Zhang W, Wang F, Shen R, Ye Y. Time of flight mass spectroscopy of 2, 2′, 4, 4′, 6, 6′-hexanitrostilbene under 1064 nm excitation. Proceedings of SPIE. 2017;**10173**:1017315

IntechOpen